

A Refined Cometary Fluorescence Model for the ν_3 Vibrational Band of Cyanogen : Application to JWST/NIRSPEC Spectrum

P. Hardy^{1,2}, P. Rousselot^{2,*}, C. Richard^{1,**}, V. Boudon¹, X. Landsheere³, A. Voute^{3,4}, L. Manceron^{3,4}, and F. Kwabia Tchana³

¹ Université Bourgogne Europe, CNRS, Laboratoire Interdisciplinaire Carnot de Bourgogne ICB UMR 6303, F-21000 Dijon, France

² Université Marie et Louis Pasteur, CNRS, Institut UTINAM (UMR 6213), OSU THETA, F-25000 Besançon, France

³ Université Paris Cité and Univ Paris Est Creteil, CNRS, LISA, F-75013 Paris, France

⁴ Synchrotron SOLEIL, Ligne AILES, L'Orme des Merisiers, St-Aubin BP48, 91192 Gif-sur-Yvette Cedex, France

ABSTRACT

Aims. Cyanogen (C_2N_2) was among the many molecules identified in the coma of 67P/Churyumov-Gerasimenko during the Rosetta mission. As a potential parent species of the CN radical, its abundance relative to other species such as HCN should be generalized to comets observed from ground-based facilities.

Methods. To investigate its presence from infrared spectra in other comets, we developed a new fluorescence model for the ν_3 fundamental band. From new high-resolution infrared spectra of cyanogen, we analyzed the region of the ν_3 band of C_2N_2 , centered around $4.63 \mu m$ (2158 cm^{-1}). In addition to line positions and intensities, ground and excited molecular parameters were obtained.

Results. The spectroscopic analysis allowed us to develop a new fluorescence model for cyanogen. Excitation rates of the ν_3 band of cyanogen are presented. An attempt to detect cyanogen in a high-resolution spectrum of comet C/2022 E3 (ZTF) is discussed.

Key words. comets: general – molecular data – infrared: general – techniques: spectroscopic

1. Introduction

Among the limited number of space missions dedicated to cometary science, the Rosetta spacecraft launched in 2004 significantly enhanced the understanding of those small bodies, by conducting a two-year study of the comet 67P/Churyumov-Gerasimenko. One of Rosetta's instruments, the mass spectrometer ROSINA, discovered numerous chemical species in the coma that had never been observed in comets before.

One such species, cyanogen (C_2N_2) is a linear molecule that was previously only observed in the atmosphere of Titan by Kunde et al. (1981) before its detection on comet 67P (Altwegg et al. 2019). Although the CN radical is a prominent feature in cometary optical spectra, its origins (i.e., its corresponding parent species) are still poorly understood. In particular, hydrogen cyanide (HCN) has been shown not to be the only source of cometary CN (Hänni et al. (2020), Hänni et al. (2021)). C_2N_2 , while being much less abundant than HCN in the coma of comet 67P (Hänni et al. (2021) reported $C_2N_2/HCN = 0.0018 \pm 0.0009$, (1.24-1.74 au)) could still participate in the formation of CN. Its detection in 67P should be extended to other comets to better constrain its abundance in cometary environments.

In this context, we study one of the fundamental bands of cyanogen, centered at 2158 cm^{-1} ($4.63 \mu m$). After discussing experimental details (Section 2) and theoretical aspects (Section 3), we present both the results of our spectroscopic analysis in Section 4 and the development of a fluorescence model adapted to comets in Section 5. Finally, our results and a tentative detection in comet C/2022 E3 (ZTF) is presented in Section 6.

2. Experimental details

Seven absorption spectra of cyanogen have been recorded in the range from 1800 to 3500 cm^{-1} using the high-resolution Bruker IFS125HR FTS located at the LISA facility in Créteil (France). The instrument was equipped with a silicon carbide Globar source, a KBr/Ge beamsplitter and a liquid nitrogen-cooled Indium Antimonide (InSb) detector. The InSb detector was used in conjunction with an optical filter, with a bandpass of $1800\text{--}3400 \text{ cm}^{-1}$, to minimize the size of the interferogram data files and also to improve the signal-to-noise ratio. The FTS was continuously evacuated below $3 \times 10^4 \text{ hPa}$ by a turbomolecular pump to minimize absorption by atmospheric gases. The diameter of the entrance aperture of the spectrometer was set to 1.3 mm to maximize the intensity of infrared radiation falling onto the InSb detector without saturation or loss of spectral resolution. Interferograms were recorded with an 80 kHz scanner frequency and a maximum optical path difference (MOPD) of 250 cm . According to the Bruker definition (resolution = $0.9/\text{MOPD}$), this corresponds to a resolution of 0.0036 cm^{-1} . The spectra were obtained by Fourier transformation of the interferograms using a Mertz phase correction with a 1 cm^{-1} resolution, a zero-filling factor of 2 and no apodization (boxcar option). The cyanogen (C_2N_2) sample was synthesized in the laboratory by progressive heating of silver cyanide (99%, Sigma Aldrich) in a glass bulb previously evacuated:



About five grams of silver cyanide powder were placed in a thoroughly cleaned, grease-free glass bulb and heated gently under high vacuum up to 200°C to eliminate atmospheric gases and adsorbed water vapor. Next, the powder was progressively

* cyril.richard@ube.fr

** phil@obs-besancon.fr

#	C ₂ N ₂ Pressure (hPa)	Number of scans
S1	0.9968 (50)	1460
S2	1.3404 (67)	1310
S3	1.8718 (94)	1430
S4	2.337 (12)	1410
S5	2.673 (13)	1480
S6	3.335 (17)	1250
S7	4.003 (20)	1250

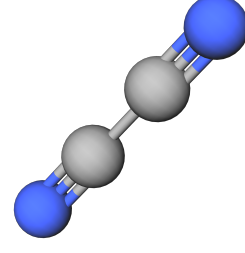


Fig. 1: Representation of the cyanogen molecule, where Carbons are represented in gray, Nitrogens in blue.

Table 1: Pressure of C₂N₂ (in hPa) and number of interferograms averaged to yield the corresponding spectrum (number of scans). All the spectra were recorded with an absorption optical path of 0.849(2) m, at a stabilized room temperature of 293 ± 1 K, a resolution (equal to 0.9 divided by the maximum optical path difference) of 0.0036 cm⁻¹ and an entrance aperture diameter of the interferometer equal to 1.3 mm. The absolute uncertainty on the pressure is equal to 0.5% of the value given.

heated to 300°C where evolution of cyanogen gas slowly started to occur. The first batch, containing traces of carbon dioxide from carbonate impurities, was discarded and further heating to about 400°C completed the reaction and cyanogen was collected in a glass trap on the vacuum line. Finally, a trap-to-trap distillation at about -70°C helped reduce possible remaining impurities (HCN, CO₂ or others). The remaining CO₂ traces were estimated from IR measurements to much less than 0.1%.

A short-path absorption cell (SPAC) made of Pyrex glass and equipped with CsBr windows was used for all the measurements. The SPAC is a White-type multipass cell with a base length of 0.20 m. In this experiment, an optical path of 0.849(2) m was used. The sample pressure in the cell was measured using calibrated MKS Baratron capacitance manometers models 627 (2.6664 hPa full scale) and 628 D (13.332 hPa full scale) characterized by a stated reading accuracy of 0.12%. Considering the uncertainty arising from small variations of the pressure during the recording (< 0.35%), we estimated the measurement uncertainty on the pressure to be equal to 0.5%. All the spectra were recorded at a stabilized room temperature of 293 ± 1 K. The following procedure was used to record the spectra. A background spectrum was first collected while the cell was being continuously evacuated. It was recorded at the same resolution as the sample spectra to ensure proper removal of the H₂O or CO₂ absorption lines. The infrared gas cell was then passivated several times with the C₂N₂ sample. Finally, spectra were recorded for seven different sample pressures of cyanogen. The seven pressures chosen and the number of interferograms recorded and averaged to yield the corresponding spectra are listed in Table 1. All the sample spectra were ratioed against the empty cell background spectrum, and interpolated 4 times. The root-mean-square signal-to-noise ratio in the ratioed spectra ranged between 1200 and 1900. The spectrum was calibrated by matching the measured positions of 25 lines of residual CO₂ and H₂O observed therein to reference wavenumbers available in HITRAN (Gordon et al. (2022)) with a root-mean-square (RMS) deviation of 0.00018 cm⁻¹. The absolute accuracy of the measured C₂N₂ line positions was estimated as the square root of the sum of squares of the accuracy of the reference CO₂ and H₂O line positions in HITRAN (better than 0.0001 cm⁻¹) plus the RMS deviation between the observed frequencies and values listed in HITRAN for CO₂ and H₂O, yielding in total 0.0002 cm⁻¹.

Symmetry	Degeneracy (ω)	Vibration mode	Band center (cm ⁻¹)
Σ_g	1	ν_1 : CN symmetric-stretch	2330.4859
Σ_g	1	ν_2 : NN symmetric-stretch	845.5939*
Σ_u	1	ν_3 : CN asymmetric-stretch	2157.8243
Π_g	2	ν_4 : CCN bend	502.7745*
Π_u	2	ν_5 : CCN bend	233.7225

Table 2: Fundamental levels of cyanogen, obtained from Shimanouchi (1977). Band centers values come from the analysis of Maki (2011). The asterisk for ν_2 and ν_4 band centers indicate that the levels are infrared inactive.

3. Theoretical aspects

Cyanogen (represented in Fig. 1) belongs to the D_{∞v} point. Its five fundamental vibrational levels (taken from Shimanouchi (1977) and Maki (2011)) are summarized in Table 2.

The allowed frequencies are obtained as

$$\nu_J = \nu_0 + E_u(J_u) - E_l(J_l), \quad (2)$$

where the subscripts u and l refer to the upper and lower vibrational levels, respectively. In our case, the upper level corresponds to ν_3 , while the lower level is the ground-vibrational state. ν_0 is the frequency of the pure vibrational transitions, J is the rotational angular momentum quantum number, and E is the rotational energy (Herzberg 1960):

$$E(J) = BJ(J+1) - DJ^2(J+1)^2 + HJ^3(J+1)^3 + \dots, \quad (3)$$

with B the rotational constant, D the quartic centrifugal distortion constant, and H the sextic centrifugal constant. For states different from Σ , the non-zero perpendicular component of the angular momentum interact with the rotational motion of the molecule, leading to a splitting (Λ) of energy levels whose intensity increases as J increases:

$$\Lambda(J) = qJ(J+1) + q_D J^2(J+1)^2 + q_H J^3(J+1)^3 + \dots \quad (4)$$

For one given J , two states exist: the former corresponding to a symmetric wavefunction (noted e), the latter corresponding to an antisymmetric wavefunction (noted f), and the energies are given by:

$$E_e(J) = E(J) + \frac{\Lambda(J)}{2}, \quad (5)$$

$$E_f(J) = E(J) - \frac{\Lambda(J)}{2}. \quad (6)$$

This effect is known as the Λ -doubling. The smaller the splitting, the more challenging it becomes to resolve the two lines at low J values, given the limited spectrum's resolution.

Temperature (K)	Q_R	Q_V	Q
50	997.0551	1.0024	999.4530
100	1992.7268	1.0746	2141.3953
150	2988.5176	1.2727	3803.4749
200	3984.4273	1.5978	6366.2388
250	4980.4558	2.0653	10285.9925
300	5976.6032	2.7033	16156.3476

Table 3: Values of rotational (Q_R), vibrational (Q_V), and roto-vibrational (Q) partition function at different temperatures.

Line intensities S_J are given by [Rothman & Young \(1981\)](#)

$$S_J = \varepsilon_J \frac{\nu_J}{\nu_0} L_J \frac{S_\nu}{Q_r} (e^{-hcE_i/kT})(1 - e^{-hc\nu_J/kT})(1 + A_1 m)^2. \quad (7)$$

In this expression, ε_J is the statistical weight of level J , L_J is the Hönl-London factor (or relative intensity), S_ν is the band strength (usually given in $\text{cm}^{-2} \text{atm}^{-1}$), and Q_r is the rotational partition function. The last term is the first-order Herman-Wallis correction, which is equal to 1 for perfect rigid rotors. This correction depends on m , defined as $J + 1$ for the R -branch, J for the Q -branch, and $-J$ for the P -branch. For linear (and diatomic) molecules, the Hönl-London factors in the lower state are simply given by ([Herzberg \(1950\)](#))

$$L_J = |m|. \quad (8)$$

For the main isotopologue ($^{14}\text{N}^{12}\text{C}^{12}\text{C}^{14}\text{N}$, with an abundance of 97.08% reported in [Gordon et al. \(2022\)](#)), ε_J is equal to 6 for even J values; 3 for odd J values. In practice, these statistical weights lead to an intensity alternation between two consecutive lines in the spectra. The rotational partition function appearing in equation 7 is expressed as

$$Q_R = \sum_{J=0}^{\infty} \varepsilon_J (2J + 1) e^{-hcE_i(J)/kT}, \quad (9)$$

while the vibrational partition function is given by

$$Q_V = \prod_{i=1}^5 (1 - e^{-hc\nu_{0,i}/kT})^{-d_i}. \quad (10)$$

The roto-vibrational partition function (Q) is the product of Q_R and Q_V . The values of the partition function at different temperatures are given in Table 3.

To derive the excitation rates, we followed the development presented in [Russo et al. \(2001\)](#). The Einstein coefficient A_ν for a vibrational band ([Crovisier & Encrenaz \(1983\)](#), [Crovisier \(1984\)](#)) is defined by :

$$A_\nu = \frac{3.080 \times 10^{-8} (T_\nu/300) \nu_0^2 S_\nu Q_V}{\omega}, \quad (11)$$

where T_ν is the temperature at which the band intensity is obtained, and ω is the band degeneracy (indicated for the fundamental levels of cyanogen in Table 2). The g-factor for a fundamental band excited by a blackbody of solid angle Ω at temperature T_b is then expressed ([Crovisier & Encrenaz \(1983\)](#)):

$$g_\nu = \frac{\omega \Omega}{4\pi} A_\nu (e^{hc\nu_0/kT_b} - 1)^{-1}. \quad (12)$$

With an excitation by the Sun at 1 au, $T_b=5770$ K and $\Omega/4\pi = 5.42 \times 10^{-6}$ ([Russo et al. \(2001\)](#)).

4. Spectroscopic analysis

4.1. Positions

Using the PGOPHER software ([Western \(2017\)](#)), we analyzed the experimental spectra of C_2N_2 from 2120 cm^{-1} to 2185 cm^{-1} . The S2 experimental spectrum ($P=1.3404(67)$ hPa) is represented in Fig. 2. In addition to the ν_3 fundamental band (also written as $\nu_3 - \text{GS}$, where GS stands for Ground State), some absorption lines from hot bands are also present in the spectrum: we identified $\nu_3 + \nu_4 - \nu_4$, $\nu_3 + \nu_5 - \nu_5$, and $\nu_3 + 2\nu_5 - 2\nu_5$. Energy levels and the four transitions discussed hereafter are shown in Fig. 3. As ν_4 , ν_5 and $2\nu_5$ are the lowest excited energy levels of C_2N_2 , these hot bands are pretty strong and affected the study of the fundamental band ν_3 , because hot bands lines are often blended with ν_3 lines. In this context and because they were fairly easy to assign, we decided to include the hot bands in this work, even though the fluorescence model described later only focus on the fundamental band, as it is supposed to be the main component in cold environments such as the coma of a comet. We started our analysis in PGOPHER using spectroscopic parameters from [Maki \(2011\)](#).

For the $\nu_3 - \text{GS}$ band, 201 lines have been assigned from $J = 0$ to $J = 112$. A few lines have been systematically removed from the fit if they were obviously blended with other lines, and decreased the quality of the fit. The average error d_{RMS} , defined as

$$d_{RMS} = \sqrt{\frac{\sum_i d_i^2}{n}}, \quad (13)$$

where n is the number of observations, and d_i is the difference in cm^{-1} between the observed and calculated position of line i . In our fit of the fundamental band ν_3 , $d_{RMS} = 1.21 \times 10^{-4} \text{ cm}^{-1}$. For the hot band $\nu_3 + 2\nu_5 - 2\nu_5$, 114 lines have been assigned, from $J = 1$ to $J = 99$, with $d_{RMS} = 2.43 \times 10^{-4} \text{ cm}^{-1}$. ν_3 and $\nu_3 + 2\nu_5$ are both Σ_u^+ states, meaning there are no Λ -doubling observed for those two bands. This is not the case for $\nu_3 + \nu_4$ and $\nu_3 + \nu_5$, which are respectively Π_u and Π_g states. As lines are blended for low J (because the splitting is not big enough), we did not include lines with $J < 11$ for $\nu_3 + \nu_5 - \nu_5$ and $J < 14$ for $\nu_3 + \nu_4 - \nu_4$ while fitting positions. The evolution of the splitting as J increases is illustrated in Fig. A.2.

For $\nu_3 + \nu_4 - \nu_4$, we fitted 195 lines from $J = 13$ to $J = 85$, with $d_{RMS} = 2.34 \times 10^{-4} \text{ cm}^{-1}$. For $\nu_3 + \nu_5 - \nu_5$, we fitted 323 lines from $J = 10$ to $J = 96$, with $d_{RMS} = 1.46 \times 10^{-4} \text{ cm}^{-1}$. The fit residuals for the line positions of each band discussed are represented in Fig. 4, 5, 6 and 7. Residuals are plotted against the upper level rotational quantum number J , to highlight potential non-zero higher-terms in the polynomial expansion of the energy states. The total average error (considering the four bands together) is $1.8 \times 10^{-4} \text{ cm}^{-1}$, and all the fit residuals are represented in Fig. 8, where the x-axis is now the wavenumber in cm^{-1} .

The spectroscopic parameters derived from the fit in positions are summarized in Table 4. The standard deviation is indicated in parentheses. No parentheses indicate that the value was fixed using values from [Maki \(2011\)](#).

4.2. Intensities

We restricted our intensity analysis to the $\nu_3 - \text{GS}$ band, as the cometary fluorescence model will focus only on this band. The fit was done using the MSFP (Multi-Spectrum Fitting Program),

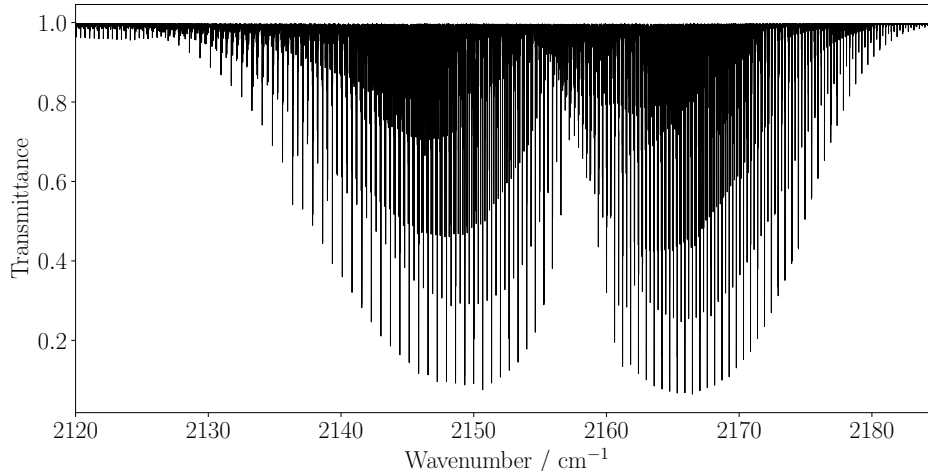


Fig. 2: Experimental high-resolution spectrum of C_2N_2 between 2120 and 2185 cm^{-1}

	Origin	B	D	H	L	q	qD	qH	qL							
GS (Σ_g^-)	0	0.1570879982(2801)	2.11469(189)	$\times 10^{-8}$	0	0	0	0	0							
ν_3 (Π_u)	233.7225 ^a	0.1576278497(3905)	2.222624(8402)	$\times 10^{-8}$	1.1146(5439)	$\times 10^{-14}$	0	-2.212580(4536)	$\times 10^{-4}$	4.129(387)	$\times 10^{-10}$	0	0			
$2\nu_3$ (Σ_g^+)	464.8685 ^a	0.158166967(1048)	4.20455(5699)	$\times 10^{-8}$	9.153(1175)	$\times 10^{-13}$	-1.7012(8007)	$\times 10^{-17}$	0	0	0	0				
ν_4 (Π_u)	502.7745 ^a	0.1574531178(2931)	2.15394(332)	$\times 10^{-8}$	0	0	-1.17900(1700)	$\times 10^{-4}$	-3.3476(8270)	$\times 10^{-9}$	5.628(1551)	$\times 10^{-13}$	-3.3370(9800)	$\times 10^{-17}$		
ν_3 (Σ_u^-)	2157.824256(34)	0.1565544657(2892)	2.101485(3062)	$\times 10^{-8}$	-6.649(2975)	$\times 10^{-15}$	3.00(132)	$\times 10^{-19}$	0	0	0	0				
$\nu_3 + \nu_4$ (Π_g)	2389.736280(30)	0.1570968635(3867)	2.214595(8253)	$\times 10^{-8}$	9.869(5294)	$\times 10^{-15}$	0	-2.186458(4525)	$\times 10^{-4}$	3.904(383)	$\times 10^{-10}$	0	0			
$\nu_3 + 2\nu_5$ (Σ_u^-)	2619.092571(39)	0.157638754(1055)	4.17941(5716)	$\times 10^{-8}$	9.163(1170)	$\times 10^{-13}$	-1.8518(7922)	$\times 10^{-17}$	0	0	0	0				
$\nu_3 + \nu_4$ (Π_u)	2657.530013(67)	0.1569204218(3257)	2.160948(8013)	$\times 10^{-8}$	3.876(1410)	$\times 10^{-14}$	-3.061(958)	$\times 10^{-18}$	-1.17655(1709)	$\times 10^{-4}$	-3.2873(8441)	$\times 10^{-9}$	5.4587(16123)	$\times 10^{-13}$	-3.192(1040)	$\times 10^{-17}$

Table 4: Derived parameters from the lines positions analysis in PGOHER. Uncertainties are indicated in parentheses, in units of the last digits. *B*: rotational constant, *D*: J^4 centrifugal distortion, *H*: J^6 centrifugal distortion, *L*: J^8 centrifugal distortion, *q*: lambda-doubling constant, *qD*: J^4 centrifugal distortion of *q*, *qH*: J^6 centrifugal distortion of *q*, *qL*: J^8 centrifugal distortion of *q*. ^afixed values coming from Maki (2011), all values are in units of cm^{-1} .

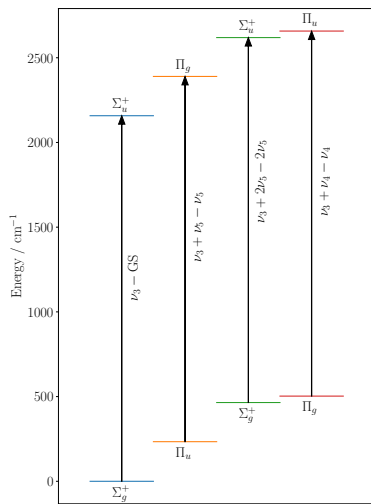


Fig. 3: The four vibrational bands presented in this work: $\nu_3 + \nu_4 - \nu_5$, $\nu_3 + \nu_5 - \nu_5$, and $\nu_3 + 2\nu_5 - 2\nu_5$. Symmetries are labeled for each energy levels.

developed by Jean Vander Auwera at Université Libre de Bruxelles. This program takes as input the spectra recorded under different conditions, the total internal partition function of the con-

sidered species, and the linelists to be fitted. We measured the intensity and self-broadening coefficients of 147 lines of the band $\nu_3 - GS$ by fitting Voigt profiles. As an example, the line $R(53)$ is represented for three different pressures (S2, S3, S4) in Fig. 9. We did not include lines known to be blended with absorption lines originating from the three hot bands discussed earlier because the measured lines intensity and broadening are overestimated in those cases. From the measurements and the intensity formula (equation 7), we have derived the band strength of $\nu_3 - GS$: $S_{\nu_3} = 18.328 \pm 0.071 \text{ cm}^{-2} \text{ atm}^{-1}$ ($S_{\nu_3} = 18.5 \text{ cm}^{-2} \text{ atm}^{-1}$ in Bockelee-Morvan & Crovisier (1985)). The first term in the Herman-Wallis correction was also derived, and we found $A_1 = 53.4 \pm 6.2 \times 10^{-5}$. The comparison between the measured intensities and the calculated intensities is represented in Fig. A.1. The intensity fit has a root mean square deviation equal to 6.383%.

5. Development of a cometary fluorescence model

5.1. Ground-state population and energy levels

From our analysis, we first computed the energy levels E_J of cyanogen in the ground state (equation 3). As a parent species, it is assumed that the initial population of C_2N_2 is mainly in the ground state. This is because the temperature in the coma is very low (typically a few tens of kelvin), and the sublimation of the parent species from the nucleus to the coma does not excite the molecules to higher vibrational states. Moreover, in a first good approximation, collisions are negligible because the coma is an optically thin environment. The initial population distribution in the ground state follows:

$$N_J = \varepsilon_J (2J + 1) e^{-hcE_J/kT}, \quad (14)$$

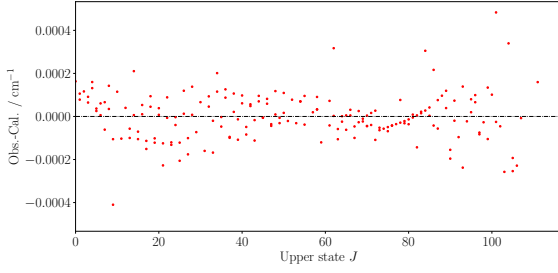


Fig. 4: Fit residuals (in red) for the line positions of the $\nu_3 - \text{GS}$ band of C_2N_2 with respect to the upper state rotational quantum J . 190 observations, with an average error of $1.10 \times 10^{-4} \text{ cm}^{-1}$.

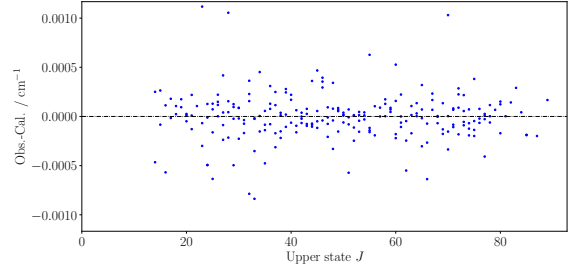


Fig. 5: Fit residuals (in blue) for the line positions of the $\nu_3 + \nu_4 - \nu_4$ band of C_2N_2 with respect to the upper state rotational quantum J . 234 observations, with an average error of $2.44 \times 10^{-4} \text{ cm}^{-1}$.

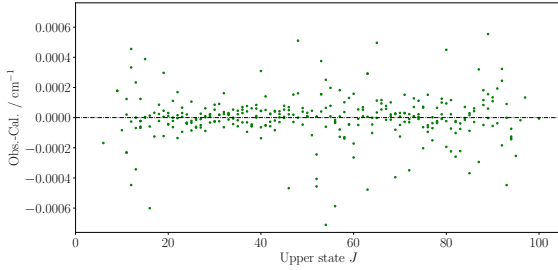


Fig. 6: Fit residuals (in green) for the line positions of the $\nu_3 + \nu_5 - \nu_5$ band of C_2N_2 with respect to the upper state rotational quantum J . 319 observations, with an average error of $1.53 \times 10^{-4} \text{ cm}^{-1}$.

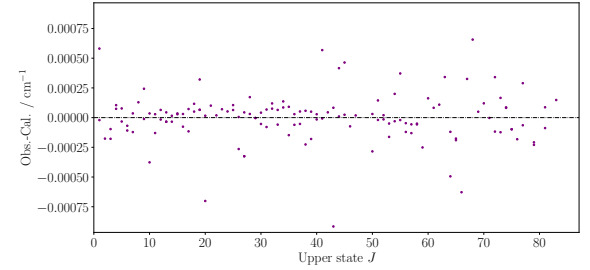


Fig. 7: Fit residuals (in purple) for the line positions of the $\nu_3 + 2\nu_5 - 2\nu_5$ band of C_2N_2 with respect to the upper state rotational quantum J . 137 observations, with an average error of $2.06 \times 10^{-4} \text{ cm}^{-1}$.

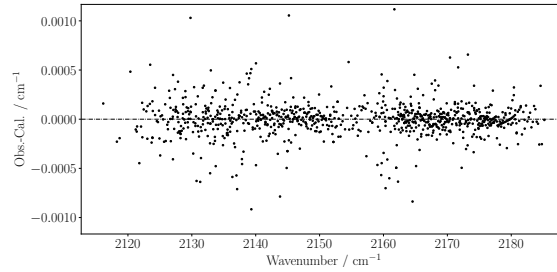


Fig. 8: Fit residuals (in black) for the line positions of the four bands of C_2N_2 presented in this work, with respect to the wavenumber in cm^{-1} . 880 observations, with an average error of $1.83 \times 10^{-4} \text{ cm}^{-1}$.

and the initial fractional population f_J is the ratio between N_J and the total partition function Q at temperature T .

$$f_J = \frac{N_J}{Q}$$

5.2. Branching ratio from the ground state to ν_3

The population of the upper state ν_3 is determined using branching ratios, defined as:

$$Br(J) = \frac{L_J}{2J+1} \times (1 + A_1 m)^2, \quad (16)$$

which we develop as:

$$Br(J; \Delta J = -1) = \frac{J}{2J+1} \times (1 - A_1 J)^2, \quad (17)$$

$$(15) \quad Br(J; \Delta J = +1) = \frac{J+1}{2J+1} \times (1 + A_1 (J+1))^2. \quad (18)$$

In absorption, $\Delta J = -1$ corresponds to the P -branch, while $\Delta J = +1$ corresponds to the R -branch. The populated J level in the ground state is split to J (P -branch) or $J+1$ (R -branch) level of the ν_3 excited level, following usual selection rules for rovibrational transitions of linear molecules:

$$\begin{aligned} \Delta \Lambda &= 0, \pm 1, \\ \Delta J &= \pm 1, & \text{if } \Delta \Lambda = 0, \Lambda = 0, \\ \Delta J &= 0, \pm 1 & \text{else.} \end{aligned} \quad (19)$$

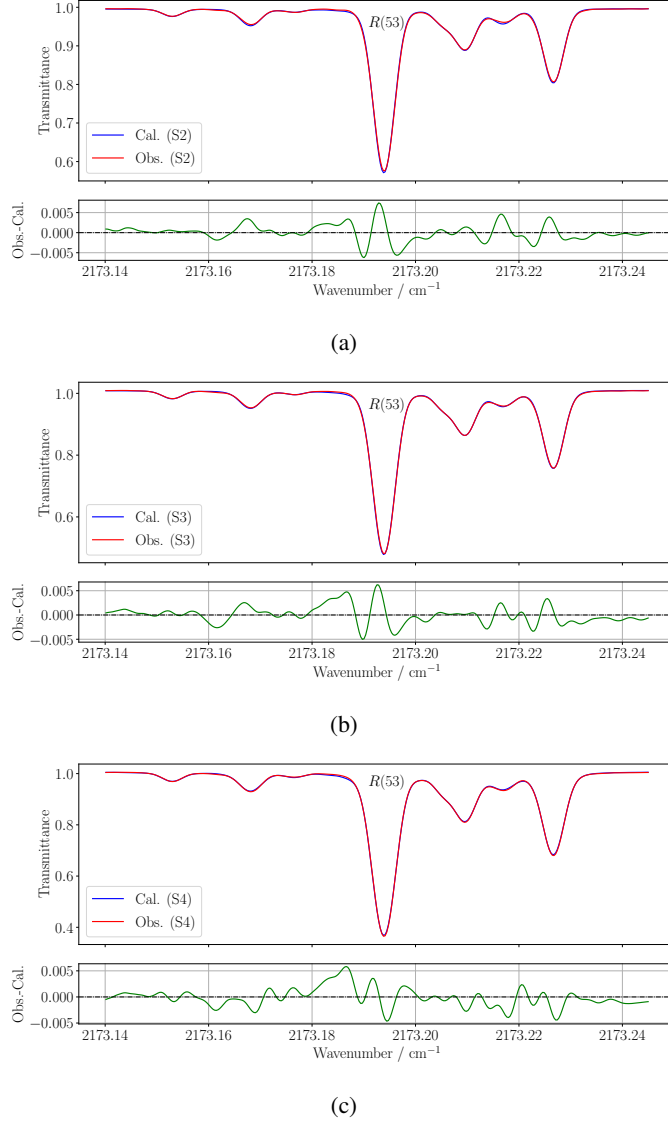


Fig. 9: Simulation (in red) and observation (in blue) of the ν_3 $R(53)$ line of C_2N_2 in the S2 (a), S3 (b), S4 (c) spectra. Residuals are shown in green for each case.

In our case, ν_3 and GS being both Σ states, $\Delta\Lambda = 0$, $\Lambda = 0$, and the Q -branch is forbidden. The fractional population $f_{J'}$ in the excited state J' is then:

$$f_{J'} = Br(J = J' - 1; \Delta J = +1)f_{J'=J'-1}, \quad (20)$$

$$+ Br(J = J' + 1; \Delta J = -1)f_{J'=J'+1}. \quad (21)$$

As an example, the excited $J' = 1$ level is populated from the ground states $J = 0$ and $J = 2$, and

$$f_{J'=1} = Br(J = 0; \Delta J = +1)f_{J=0}, \quad (22)$$

$$+ Br(J = 2; \Delta J = -1)f_{J=2}. \quad (23)$$

This is illustrated by green arrows in Fig. 10. Values for E_J , f_J and $E_{J'}$, $f_{J'}$ up to $J = 20$ at $T = 50$ K are presented in Table 5.

Finally, the population which falls back from the excited J' level in the Ground State through the R -branch or P -branch is :

$$f_{J'',R} = Br(J' = J'' + 1; \Delta J = -1)f_{J'=J''+1}, \quad (24)$$

$$f_{J'',P} = Br(J' = J'' - 1; \Delta J = +1)f_{J'=J''-1}, \quad (25)$$

where ΔJ is now defined as $J'' - J'$. This unusual choice in spectroscopy (where ΔJ is normally $J' - J''$) was made to stay consistent with equations 17 and 18. The corresponding emission g -factors are obtained by multiplying $f_{J''}$ by the g -factor of the band (defined in equation 12):

$$g_{J'',R} = f_{J'',R} \times g_\nu, \quad (26)$$

$$g_{J'',P} = f_{J'',P} \times g_\nu. \quad (27)$$

6. Results and discussion

6.1. Excitation rates

For the ν_3 band, considering an excitation by the Sun at 1 au, $g_\nu = 5.22 \times 10^{-5}$ photons s^{-1} molecule $^{-1}$, a value 50% higher than the one reported in [Bockelee-Morvan & Crovisier \(1985\)](#), despite reporting a similar band strength. We explain this difference by an underestimation of the vibrational partition function Q_ν in [Bockelee-Morvan & Crovisier \(1985\)](#), impacting the Einstein coefficient of the band and therefore the g -factor of the band (respectively equations 11 and 12). At 300 K, $Q_\nu = 1.819$

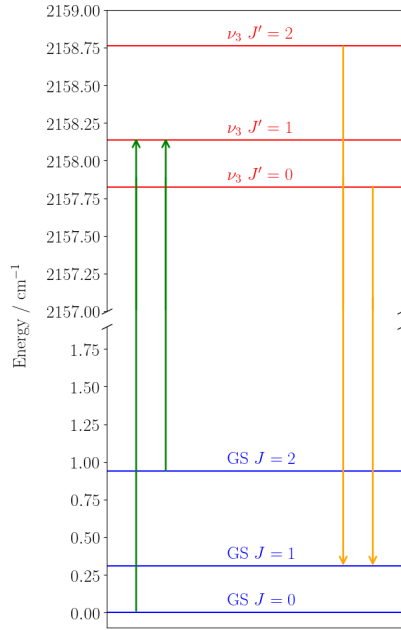


Fig. 10: Schematic representation of the fluorescence process. The pumping from GS to ν_3 is represented in green, and the pumping from ν_3 to GS is represented in orange. The y-axis has been broken for clarification.

J/J'	GS		ν_3	
	E_J	f_J	$E_{J'}$	$f_{J'}$
0	0.00	0.00600	2157.82	0.00297
1	0.31	0.00892	2158.14	0.01767
2	0.94	0.02921	2158.76	0.01446
3	1.89	0.01990	2159.70	0.03943
4	3.14	0.04936	2160.96	0.02446
5	4.71	0.02883	2162.52	0.05717
6	6.60	0.06455	2164.40	0.03202
7	8.80	0.03496	2166.59	0.06941
8	11.31	0.07370	2169.10	0.03662
9	14.14	0.03797	2171.91	0.07552
10	17.28	0.07668	2175.04	0.03817
11	20.74	0.03801	2178.49	0.07577
12	24.51	0.07414	2182.25	0.03699
13	28.59	0.03560	2186.32	0.07114
14	32.99	0.06738	2190.70	0.03371
15	37.70	0.03145	2195.40	0.06302
16	42.73	0.05793	2200.41	0.02907
17	48.07	0.02635	2205.73	0.05298
18	53.72	0.04734	2211.36	0.02384
19	59.69	0.02101	2217.31	0.04241
20	65.97	0.03687	2223.57	0.01864

Table 5: Energy levels and fractional population of C_2N_2 in the ground state (GS) and in the ν_3 excited state, with $T = 50$ K.

in [Bockelee-Morvan & Crovisier \(1985\)](#), while we have $Q_v = 2.703$ and [Fayt et al. \(2012\)](#) have $Q_v = 2.70687$. Excitation rates up to $J = 20$ for $T = 50$ K are presented in Table 6, and represented in Fig. 11.

Line	Wavenumber/cm ⁻¹	$g_{J'}/10^{-6}\text{s}^{-1}\text{molecule}^{-1}$	Line	Wavenumber/cm ⁻¹	$g_{J'}/10^{-6}\text{s}^{-1}\text{molecule}^{-1}$
P(20)	2151.3387	1.126	R(0)	2158.1374	0.312
P(19)	2151.6730	0.634	R(1)	2158.4494	0.307
P(18)	2152.0063	1.414	R(2)	2158.7604	0.897
P(17)	2152.3386	0.778	R(3)	2159.0703	0.577
P(16)	2152.6697	1.691	R(4)	2159.3791	1.382
P(15)	2152.9999	0.907	R(5)	2159.6869	0.787
P(14)	2153.3289	1.922	R(6)	2159.9936	1.726
P(13)	2153.6569	1.003	R(7)	2160.2992	0.919
P(12)	2153.9839	2.064	R(8)	2160.6038	1.910
P(11)	2154.3097	1.045	R(9)	2160.9072	0.972
P(10)	2154.6346	2.080	R(10)	2161.2097	1.939
P(9)	2154.9583	1.015	R(11)	2161.5110	0.951
P(8)	2155.2810	1.941	R(12)	2161.8113	1.837
P(7)	2155.6026	0.905	R(13)	2162.1105	0.874
P(6)	2155.9232	1.639	R(14)	2162.4086	1.639
P(5)	2156.2427	0.715	R(15)	2162.7056	0.758
P(4)	2156.5612	1.187	R(16)	2163.0016	1.386
P(3)	2156.8785	0.458	R(17)	2163.2965	0.625
P(2)	2157.1948	0.622	R(18)	2163.5903	1.115
P(1)	2157.5101	0.157	R(19)	2163.8830	0.491

Table 6: Wavenumbers and excitation rates (g -factors, noted $g_{J'}$) of 40 lines with $J \leq 20$ calculated at $T = 50$ K and considering a Sun illumination at 1 au. Excitation rates are expressed in photons $\text{s}^{-1}\text{molecule}^{-1}$. The excitation rate of the whole ν_3 band is $g_v = 5.22 \times 10^{-5}$ photons $\text{s}^{-1}\text{molecule}^{-1}$.

6.2. Investigation in comet C/2022 E3 (ZTF)

The Oort cloud comet C/2022 E3 (ZTF) was discovered on 2 March 2022 by the Zwicky Transient Facility. It reached perihelion in January 2023, at around 1.11 AU, with a peak magnitude of 5 ([Bolin et al. \(2022\)](#)). The comet was observed by JWST between 28 February and 4 March 2023, with $r_h \sim 1.3$ au and $\Delta \sim 0.9$ au ([Milam et al. 2023](#)). We investigated the JWST/NIRSPEC spectra obtained with the G395H/F290LP grating/filters configuration, covering the 2.87–5.27 μm range through the Integral Field Unit (IFU), with a $3.0'' \times 3.0''$ field of view. The temperature of the coma was estimated by analyzing the intensity distribution of the ν_3 band of CO_2 , the strongest emission feature in the spectrum. We assumed the gas to be in local thermodynamic equilibrium (LTE), and we expect the relative population levels to follow a Boltzmann law. From HITRAN database ([Gordon et al. 2022](#)) and simulation of fluorescence spectrum in PGO-PHER [Western \(2017\)](#), we derived $T = 56$ K. This is in agreement with the gas temperature derived from radio spectroscopy of the comet in early february by [Biver, N. et al. \(2024\)](#), where $T = 60$ K. The ν_3 band of CO_2 and the simulation are represented in Fig. 12.

6.3. Haser model

The production rate Q (in molecules s^{-1}) is defined as

$$Q = \frac{4\pi\Delta^2 F_{\text{TOA}}}{\tau g h \nu f} G \quad (28)$$

where Δ is the geocentric distance (in meters), F_{TOA} is the flux at the top of the atmosphere (in W m^{-2}), corrected for atmospheric transmittance at the Doppler-shifted line frequency, τ is the lifetime (in seconds) of the molecule, g is the fluorescence efficiency (in photons per molecule s^{-1}) of the emission line, $h\nu$ is the energy (in Joules) of a photon with a wavenumber ν , and f is a geometric term representing the fraction of molecules sampled through the telescope aperture relative to the total number of molecules in the coma. We write G the growth factor of the considered species, which is the ratio between the terminal production rate and the nucleus-centered production rate ([Dello Russo et al. \(1998\)](#)). In Eq. 28, τ and g both depend on the heliocentric distance (R_h , expressed in au). However, as $g \propto R_h^{-2}$ (see Eq. 12) and $\tau \propto R_h^2$, their product is independent of the heliocentric distance.

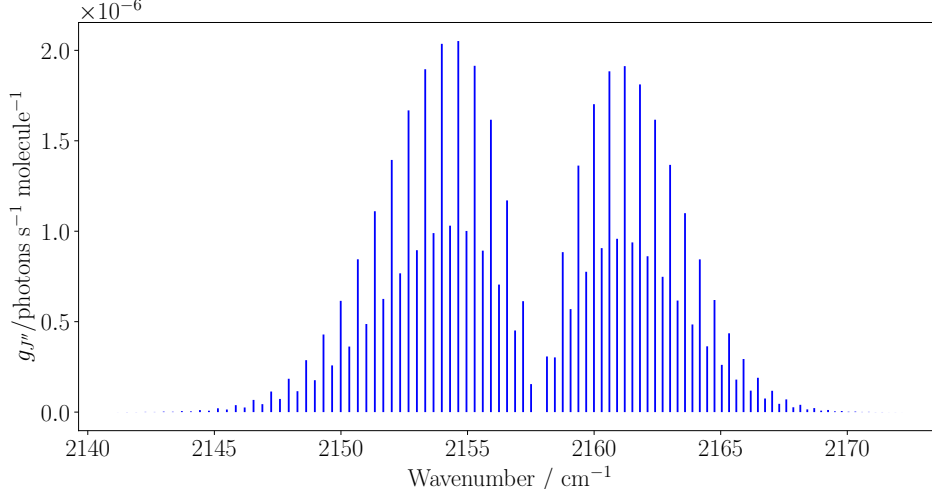


Fig. 11: Emission g -factors of C_2N_2 expressed in photons s^{-1} molecule $^{-1}$ at $T=50K$. The values are the same as in Table 6.

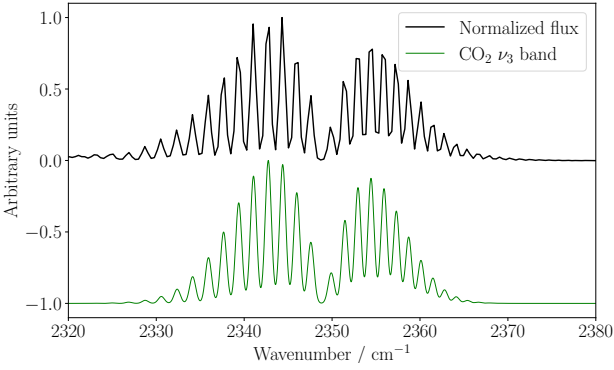


Fig. 12: JWST/NIRSPEC spectrum of comet C/2022 E3 (ZTF) (in black) between 2320 and 2380 cm^{-1} . A first order background signal (due to the scattered light on the dust) has been removed, and the spectrum has then been normalized. The intensity distribution in the band enabled us to estimate the rotational temperature of CO_2 as $T = 56$ K. In green, a synthetic fluorescence spectrum at this rotational temperature, based on data from HITRAN [Gordon et al. \(2022\)](#) and convolved taking into account the resolving power of JWST/NIRSPEC ($R \sim 2700$) is represented.

To quantify an upper limit for $Q(C_2N_2)$ in comet C/2022 E3 (ZTF), we used the Haser model ([Haser \(1957\)](#)), which describes the distribution of chemical species in the coma. It relies on the following hypothesis:

1. The cometary nucleus is assumed to be spherical, with a radius R_0 .
2. Parent species are isotropically ejected away from the nucleus, with a constant velocity noted v_0 .
3. The photodissociation of parent species is given by the law

$$n = n_0 e^{-t/\tau} \quad (29)$$

where n_0 is the number of molecules at time $t = 0$, and τ is the photodissociation lifetime of the corresponding molecule.

The density of parent species at a distance $R > R_0$ from the nucleus is given by

$$n(R) = \frac{Q}{4\pi v_0 R^2} \exp\left(-\frac{R-R_0}{\gamma}\right) \quad (30)$$

where Q is the production rate of the parent species (expressed in molecules s^{-1}) and γ is the scalelength, defined as $\gamma = v_0 \tau_0$. The column density of molecules, $N(\rho)$, is obtained by integrating $n(R)$ along the line of sight:

$$N(\rho) = \frac{Q}{4\pi v_0} \exp\left(\frac{R_0}{\gamma}\right) \int_{-\infty}^{\infty} \frac{1}{R^2} \exp\left(-\frac{R}{\gamma}\right) dz \quad (31)$$

$$= \frac{Q}{2\pi v_0 \rho} \exp\left(\frac{R_0}{\gamma}\right) \int_0^{\pi/2} \exp\left(-\frac{\rho}{\gamma \cos \alpha}\right) d\alpha \quad (32)$$

where we changed the variable of integration for α such that $\rho = R \cos \alpha$, and $dz = \rho d\alpha / \cos^2 \alpha$ (the change of variables is illustrated in Fig. A.3). We write $M(s)$ the total number of molecules for a specific parent species observed through a circular aperture s as

$$M(s) = 2\pi \int_{R_0}^R \rho N(\rho) d\rho \quad (33)$$

where we assumed that the aperture was centered on the nucleus. $R \approx \Delta \times s$ is the physical size at the comet given the geocentric distance Δ , with s in radian. The total number of molecules is obtained when $s, R \rightarrow \infty$ in Eq. 33:

$$M(\infty) = \frac{Q}{v_0} \exp\left(\frac{R_0}{\gamma}\right) \left(\gamma - \int_0^{R_0} \int_0^{\pi/2} \exp\left(-\frac{\rho}{\gamma \cos \alpha}\right) d\alpha d\rho \right) \quad (34)$$

$$\approx \frac{Q\gamma}{v_0}, \quad \text{since } R_0 \ll \gamma. \quad (35)$$

For a rectangular aperture of dimensions s_1, s_2 , centered on the nucleus,

$$M(s_1, s_2) = \left(4 \int_0^{R_2} \int_0^{R_1} N(x, y) dx dy \right) - \left(2\pi \int_0^{R_0} \rho N(\rho) d\rho \right) \quad (36)$$

where $R_1 \approx \Delta \times s_1$, $R_2 \approx \Delta \times s_2$. Again, as the second term is much smaller than the first one, the total number of molecules is approximately:

$$M(s_1, s_2) \approx 4 \int_0^{R_2} \int_0^{R_1} N(x, y) dx dy \quad (37)$$

The geometric factor f in the production rate's equation (Eq. 28) is then:

$$f = \frac{M(s_1, s_2)}{M(\infty)} \quad (38)$$

This factor depends on the slit's dimensions ($3.0'' \times 3.0''$), the radius R_0 of the cometary nucleus (we assumed $R_0 = 5$ km), the geocentric distance Δ , the lifetime τ at the heliocentric distance R_h ($\tau = \tau_{1\text{au}} \times R_h^2$) and the ejection velocity v_0 of the parent species (we chose $v_0 = 0.8 \times R_h^{-0.5}$ km s⁻¹).

The photodissociation rate of C₂N₂ at 1 au ($k = 3.08 \times 10^{-5}$ s⁻¹) was computed by [Bockelee-Morvan & Crovisier \(1985\)](#), using vacuum ultraviolet spectra from [Nuth & Glicker \(1982\)](#). This leads to a photodissociation lifetime at 1 au $\tau_{1\text{au}} = 3.25 \times 10^4$ s, which is very close to the lifetime of acetylene (C₂H₂) at 1 au ($\tau_{1\text{au}} = 3.2 \times 10^4$ s), as reported by [Crovisier & Encrenaz \(1983\)](#)

6.4. Upper limit for the production rate

We simulated synthetic spectra of C₂N₂ up to $J = 50$ to retrieve an upper limit (at 3σ -level) in the spectrum of C/2022 E3 (ZTF). We assumed the rotational temperature of C₂N₂ was equal to the rotational temperature derived with the CO₂ ν_3 band ($T_{\text{rot}} = 56$ K). We convolved the emission lines using the resolving power of JWST/NIRSPEC, choosing a Gaussian profile for the convolution. The resolution of JWST/NIRSPEC in this configuration ($R \sim 2700$) is too low to observe lines of C₂N₂ individually, as its rotational constant is low ($B \sim 0.157$ cm⁻¹). As a comparison, the much larger rotational constant of CO ($B \sim 1.922$ cm⁻¹, [Rank et al. \(1965\)](#)) leads to a much larger separation between two consecutive lines. This is illustrated in Fig. 13. We obtained $Q(\text{C}_2\text{N}_2) < 6 \times 10^{25}$ molec. s⁻¹ (3σ), where this upper limit corresponds to the maximum production rate at which the total contribution of the C₂N₂ band remains below the 3σ noise level in the JWST/NIRSPEC spectrum.

6.5. Mixing ratio estimates

From three water lines with known g-factors at $T=60$ K (summarized in Table 7) [Dello Russo et al. \(2000\)](#), we estimated the production rate of water of C/2022 E3 (ZTF) on 01/03/23 as $Q(\text{H}_2\text{O}) \sim 3 \times 10^{28}$ molec. s⁻¹.

We assumed a usual ortho to para ratio of 3, and a growth factor of 1.8. The derived value is very close to the mean production rate of water derived by [Combi et al. \(2023\)](#) (reported in [Li et al. \(2025\)](#)) one month prior to JWST measurements, when $R_h = 1.162$ au (post-perihelion): $3.05 \pm 0.06 \times 10^{28}$ molec. s⁻¹. Our upper limit on the mixing ratio of C₂N₂ is $< 0.22\%$ (3σ).

6.6. Perspectives

The high value obtained for the mixing ratio is mainly due to the low fluorescence efficiencies of C₂N₂. Despite this limiting factor, future observations may provide a more refined upper

limit, particularly if a brighter comet is observed. A higher intrinsic brightness would improve the signal-to-noise ratio, making the detection of weaker spectral features more feasible. Additionally, advancements in telescope technology will contribute to reducing uncertainties. Instruments like METIS (Mid-Infrared ELT Imager and Spectrograph), planned for installation in 2028 on the 39-meter ESO Extremely Large Telescope (ELT) [Brandl et al. \(2018\)](#), will offer high-resolution spectroscopy ($R \sim 100000$) in the L/M infrared windows. The combination of increased collecting area and improved spectral resolution could allow for better constraints on C₂N₂ production rates, offering new opportunities to probe its presence in cometary atmospheres.

7. Conclusions

This study presents a new fluorescence model for the ν_3 vibrational band of cyanogen (C₂N₂), offering a robust tool for analyzing its spectral characteristics in cometary environments. By combining high-resolution laboratory spectra with detailed theoretical modeling, we have, for the first time, derived line-by-line excitation rates for this molecule. The analysis of the ν_3 band confirms that cyanogen's fluorescence efficiency is low; however, future advancements, such as the METIS spectrometer on the ELT, are expected to significantly improve the detection and characterization of cyanogen in cometary spectra.

Cyanogen is the second molecule studied as part of the COSMIC project (COmputation and Spectroscopy of Molecules in the Infrared for Comets), following chloromethane (CH₃Cl, [Hardy et al. \(2023\)](#)). Although the ESA/Rosetta mission led to the discovery of approximately 40 new molecules, molecular databases remain incomplete, lacking data on many key species needed to analyze trace elements in cometary spectra effectively. This work highlights the importance of continued laboratory spectroscopy efforts to expand these databases and enhance our understanding of cometary chemistry, and of the origins of our solar system.

Acknowledgements. The authors are grateful to Jean Vander Auwera from Université Libre de Bruxelles for providing the MSFIT program to fit lines intensities. The COSMIC project is financed by the EIPHI Graduate School and held by ICB and UTINAM, supported by the Conseil Régional de Bourgogne Franche-Comté and the French National Research Agency (ANR).

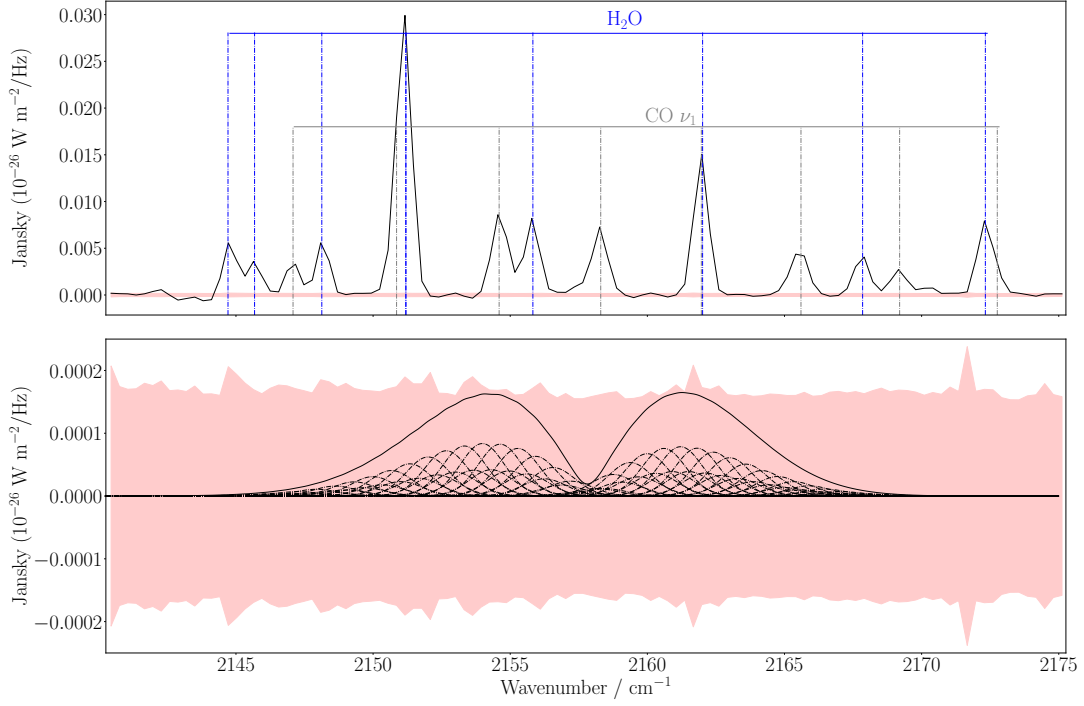


Fig. 13: *Top*: JWST/NIRSPEC spectrum of comet C/2022 E3 (ZTF) between 2140 and 2175 cm⁻¹. Emission lines of CO (ν_1) and of H₂O are represented by alternated gray and blue lines, respectively. *Bottom*: Synthetic spectrum of C₂N₂ (solid curve) calculated as the sum of ν_3 lines (dashed lines) up to $J = 50$ at $T = 56$ K, convolved by the JWST/NIRSPEC resolving power ($R \sim 2700$). The $\pm 3\sigma$ flux error envelope is represented in pink in each plot.

Band assignment	Line assignment	Rest frequency (cm ⁻¹)	g Factors at 60K (s ⁻¹)	Measured flux (Wm ⁻²)	Q_{H_2O} (s ⁻¹)
100-010	1 ₀₁ – 1 ₁₀	2039.95	7.15×10^{-7}	$2.9631(52) \times 10^{-18}$	2.96×10^{28}
001-010	0 ₀₀ – 1 ₀₁	2137.37	8.22×10^{-7}	$3.6173(46) \times 10^{-18}$	3.00×10^{28}
001-010	1 ₁₁ – 1 ₁₀	2151.19	5.70×10^{-7}	$2.5353(48) \times 10^{-18}$	3.01×10^{28}

Table 7: Emission lines of water used to estimate the water production rate in comet C/2022 E3 (ZTF) on 01/03/23. g Factors (from [Dello Russo et al. \(2000\)](#)) are expressed for $R_h = 1$ au, and assuming an ortho to para ratio of 3.

Appendix A: Additional figures

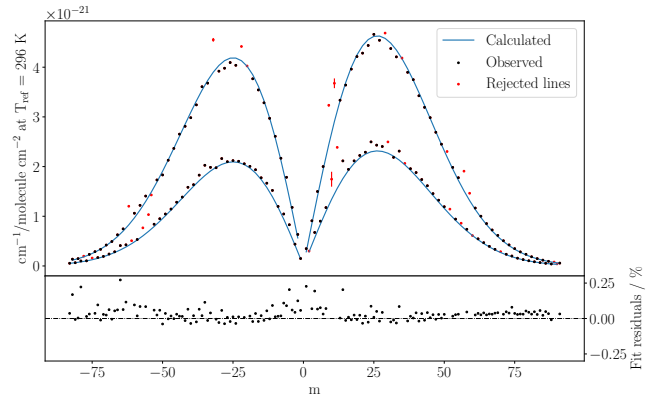
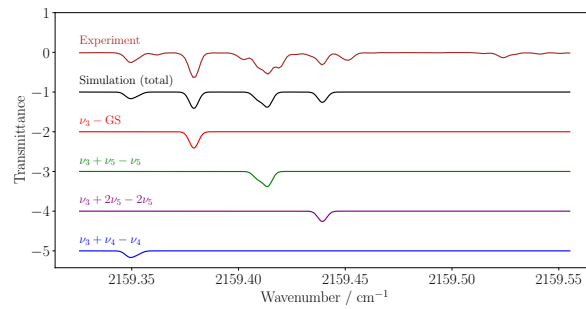
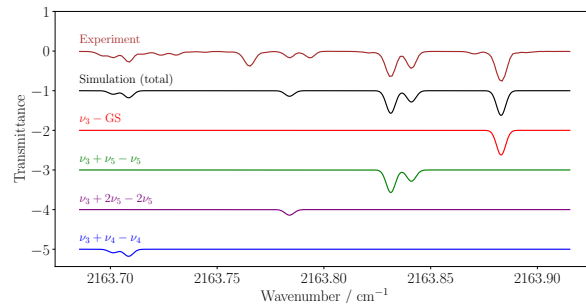


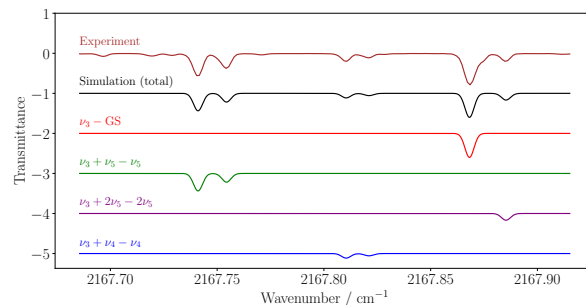
Fig. A.1: *up* Comparison between measured (dots) and calculated (blue solid lines) intensities of ν_3 – GS absorption lines with respect to m . Black points represent the 147 lines that were used to derive the band strength and the Herman-Wallis correction. We also represented the rejected lines in red: they correspond to lines blended with at least one line originating from a hot band. Error bars are displayed for each point, but are too small to be seen in most of the cases. *bottom* Fit residuals, expressed as the relative difference $((\text{Obs.}-\text{Cal.})/\text{Cal.})$, showing deviations between observed and calculated intensities.



(a) Comparison between the calculated and experimental spectrum in the region 2159.33-2159.56 cm^{-1} . The $\nu_3 + \nu_5 - \nu_5$ $R(10)$ lines (in green) and the $\nu_3 + \nu_4 - \nu_4$ $R(14)$ lines (in blue) are blended.



(b) Comparison between the calculated and experimental spectrum in the region 2163.69-2163.92 cm^{-1} . The $\nu_3 + \nu_5 - \nu_5$ $R(25)$ lines (in green) and the $\nu_3 + \nu_4 - \nu_4$ $R(29)$ lines (in blue) are separating.



(c) Comparison between the calculated and experimental spectrum in the region 2167.69-2167.92 cm^{-1} . The $\nu_3 + \nu_5 - \nu_5$ $R(39)$ lines (in green) and the $\nu_3 + \nu_4 - \nu_4$ $R(44)$ lines (in blue) are well separated.

Fig. A.2: Three regions in the R -branch with increasing rotational quantum number J (in respect to each band) from (a) to (c). The splitting of $\nu_3 + \nu_5 - \nu_5$ and $\nu_3 + \nu_4 - \nu_4$ is getting stronger as J is increasing. Some absorption lines coming from hot bands not taken into account in this work can be observed while comparing the experimental spectrum (in brown) with the total simulation (in black). An arbitrary Gaussian profile and relative intensities have been chosen to calculate the spectra in PGOPHER.

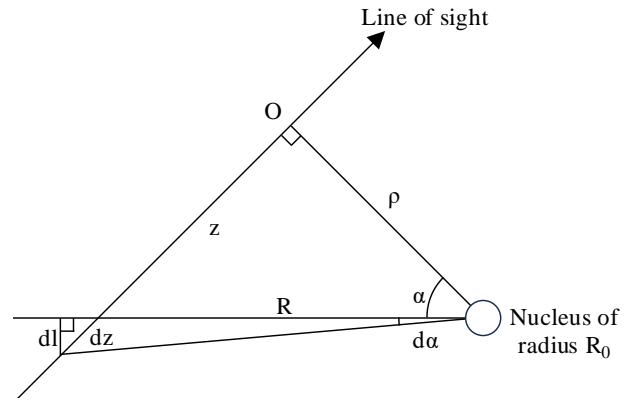


Fig. A.3: Variables used to derive the integral in equation 32. $\rho = R \cos \alpha$, $dl/R = \tan d\alpha \approx d\alpha$, and $dl/dz = \cos \alpha$. This leads to $dz = \rho / \cos^2 \alpha d\alpha$

References

- Altwegg, K., Balsiger, H., & Fuselier, S. A. 2019, *Annual Review of Astronomy and Astrophysics*, 57, 113–155
- Biver, N., Bockelée-Morvan, D., Handzlik, B., et al. 2024, *A&A*, 690, A271
- Bockelée-Morvan, D. & Crovisier, J. 1985, *A&A*, 151, 90
- Bolin, B. T., Masci, F. J., Ip, W. H., et al. 2022, *Minor Planet Electronic Circulars*, 2022-F13
- Brandl, B. R., Absil, O., Agócs, T., et al. 2018, in *Society of Photo-Optical Instrumentation Engineers (SPIE) Conference Series*, Vol. 10702, *Ground-based and Airborne Instrumentation for Astronomy VII*, ed. C. J. Evans, L. Simard, & H. Takami, 107021U
- Combi, M., Mäkinen, T., Bertaux, J.-L., Quemerais, E., & Ferron, S. 2023, in *AAS/Division for Planetary Sciences Meeting Abstracts*, Vol. 55, *AAS/Division for Planetary Sciences Meeting Abstracts #55*, 322.04
- Crovisier, J. 1984, *A&A*, 130, 361
- Crovisier, J. & Encrenaz, T. 1983, *A&A*, 126, 170
- Dello Russo, N., DiSanti, M. A., Mumma, M. J., Magee-Sauer, K., & Rettig, T. W. 1998, *Icarus*, 135, 377
- Dello Russo, N., Mumma, M. J., DiSanti, M. A., et al. 2000, *Icarus*, 143, 324
- Fayt, A., Jolly, A., Benilan, Y., et al. 2012, *Journal of Quantitative Spectroscopy and Radiative Transfer*, 113, 1195, *three Leaders in Spectroscopy*
- Gordon, I., Rothman, L., Hargreaves, R., et al. 2022, *Journal of Quantitative Spectroscopy and Radiative Transfer*, 277, 107949
- Hänni, N., Altwegg, K., Balsiger, H., et al. 2021, *A&A*, 647, A22
- Hänni, N., Altwegg, K., Pestoni, B., et al. 2020, *Monthly Notices of the Royal Astronomical Society*, 498, 2239–2248
- Hardy, P., Richard, C., Boudon, V., et al. 2023, *Journal of Quantitative Spectroscopy and Radiative Transfer*, 311, 108779
- Haser, L. 1957, *Bulletins de l'Académie Royale de Belgique*, 43, 740
- Herzberg, G. 1950, *Molecular Spectra and Molecular Structure: I. Spectra of Diatomic Molecules* (New York: Van Nostrand Reinhold)
- Herzberg, G. 1960, *Molecular Spectra and Molecular Structure: II. Infrared and Raman Spectra of Polyatomic Molecules* (New York: Van Nostrand Reinhold)
- Kunde, V. G., Aikin, A. C., Hanel, R. A., et al. 1981, *Nature*, 292, 686–688
- Li, J., Shi, J., Ma, Y., & Sun, J. 2025, *The Astronomical Journal*, 169, 126
- Maki, A. G. 2011, *Journal of Molecular Spectroscopy*, 269, 166
- Milam, S. N., Roth, N. X., Villanueva, G. L., et al. 2023, in *LPI Contributions*, Vol. 2851, *Asteroids, Comets, Meteors Conference*, 2163
- Nuth, J. A. & Glicker, S. 1982, *Journal of Quantitative Spectroscopy and Radiative Transfer*, 28, 223
- Rank, D., Pierre, A., & Wiggins, T. 1965, *Journal of Molecular Spectroscopy*, 18, 418
- Rothman, L. S. & Young, L. D. G. 1981, *Journal of Quantitative Spectroscopy and Radiative Transfer*, 25, 505
- Russo, N. D., Mumma, M. J., DiSanti, M. A., Magee-Sauer, K., & Novak, R. 2001, *Icarus*, 153, 162
- Shimanouchi, T. 1977, *Journal of Physical and Chemical Reference Data*, 6, 993
- Western, C. M. 2017, *Journal of Quantitative Spectroscopy and Radiative Transfer*, 186, 221, *satellite Remote Sensing and Spectroscopy: Joint ACE-Odin Meeting*, October 2015